Transport barriers and directed transport in the rational standard nontwist map

Rodrigo Simile Baroni **

Universidade Estadual Paulista - UNESP, Instituto de Geociências e Ciências Exatas, Departamento de Estatística, Matemática Aplicada e Computação, 13506-900, Rio Claro, SP, Brazil and Universidade de São Paulo - USP, Instituto de Física, 05508-900 São Paulo, SP, Brazil

Ricardo Egydio de Carvalho

Universidade Estadual Paulista - UNESP, Instituto de Geociências e Ciências Exatas, Departamento de Estatística, Matemática Aplicada e Computação, 13506-900 Rio Claro, SP, Brazil

José Danilo Szezech Junior O

Universidade Estadual de Ponta Grossa - UEPG, Departamento de Matemática e Estatística, 84030-900, Ponta Grossa, PR, Brazil and Universidade de São Paulo - USP, Instituto de Física, 05508-900 São Paulo, SP, Brazil

Iberê Luiz Caldas 10

Universidade de São Paulo - USP, Instituto de Física, 05508-900 São Paulo, SP, Brazil

(Received 31 October 2024; accepted 13 February 2025; published 4 March 2025)

We explore the dynamics and transport properties of the rational standard nontwist map (RSNM), which works as an extension of the standard nontwist map (SNM). In addition to the usual parameters of the SNM that govern the twist function profile and the intensity of the nonlinear perturbation, we introduce a new perturbation parameter μ in the RSNM, which makes it possible to break the symmetry of the system. The symmetry breaking leads to directed transport, known as the ratchet effect, where chaotic orbits exhibit a preferential direction of motion. We analyze the impact of μ on both the phase space and the parameter space structure, focusing on the destruction of transport barriers, which acts as separators between chaotic regions. Through numerical simulations and analysis of the fixed points stability, we demonstrate that an increase in μ enhances the chaotic volume in the lower half of the phase space, resulting in the destruction of invariant spanning curves, while simultaneously regularizing the upper half. Additionally, we explore the conditions under which partial transport barriers persist and their role in moderating transport across the phase space. We show that even small variations in a control parameter causes crossings of invariant manifolds from different regions of the phase space, enhancing transport with the mechanism of turnstiles and intercrossing. Our analysis of directed transport reveals that the breaking of symmetry by μ results in either positive or negative net transport in the phase space, depending on the control parameters. We also note that RSNM creates new regions within the parameter space, referred to as holes, due to the emergence of transport within previously null transport regions.

DOI: 10.1103/PhysRevE.111.034203

I. INTRODUCTION

Hamiltonian systems are fundamental in understanding a wide range of physical phenomena, from celestial mechanics [1–4] to plasma physics [5–8]. Within this framework, the study of area-preserving maps serves as a powerful tool for investigating chaotic dynamics and transport properties [9]. A well-known example of an area-preserving map is the Chirikov-Taylor map, or standard twist map (STM) [10], which has garnered significant interest because many nonintegrable Hamiltonian systems can be locally approximated by it [11,12]. As a result, its dynamics are often representative of the broader class of such systems. A key characteristic of the STM is that it satisfies the twist condition, which means that the rotation number changes monotonically with

the action variable. Systems that violate the twist condition are called nontwist, and many physical phenomena are modeled by such systems, as transport in atmospheric flow [13,14] and magnetic field lines and transport in plasma physics [6,15–17].

The proofs of many results of Hamiltonian nonlinear dynamics require the twist condition to be satisfied at every point of the phase space [18–21], such as the conventional KAM theorem, the Poincaré-Birkhoff theorem, and Aubry-Mather theory. Though there are KAM results for nontwist maps [22], phenomena that are typical of twist systems may not occur in nontwist systems, and new phenomena may also be observed [6,23–25]. Due to the nonmonotonicity of frequencies in nontwist systems, there are extreme values in the rotation number profile. The extreme frequency tori are known as shearless curves, which are robust transport barriers because they divide the phase space and are resilient to perturbation, roughly being the last tori to be destroyed.

^{*}Contact author: r.baroni@unesp.br

Another property of nontwist systems is the observation of orbits with the same frequency at each side of the shearless curve. This leads to twin or isochronous resonances [24], which are island chains around periodic orbits with the same period. While in twist systems the interaction of nearby separatrices of resonance islands produces a chaotic layer, a phenomenon known as Chirikov's resonance overlap criterion [18], this is not necessarily the case in nontwist systems. The separatrices of twin islands in the vicinity of the shearless curve can suffer reconnection processes that change the topology of the phase space without generating chaotic regions [6,24,25]. Twin periodic orbits can also collide and annihilate [6,25].

The question of transport in nontwist dynamics is of great interest due to the nature of the phenomena modeled by this class of systems. The quantification of the motion of collections of initial conditions in the chaotic phase space is relevant, for instance, to determine mixing rates in fluid systems [13] or particle confinement in fusion devices [5–8]. In twist systems, it is known that the remnants of broken tori—known as Cantori [26,27]—form robust partial transport barriers. The Cantori are invariant Cantor sets, and the transport through their gaps can be explained in terms of turnstiles, lobes generated by the crossing of invariant manifolds that are mapped to different phase space regions. The existence of shearless Cantori is still unproven [27], but after the breakup of a shearless barrier the transport in its vicinity can be enhanced or mitigated as the parameters are adjusted [23,28]. This phenomenon can also be analyzed by means of the turnstiles [23,28,29].

One of the most studied nontwist system is the standard nontwist map (SNM) [13,25], which has been extensively used to explore the general behavior of transport barriers, chaotic seas, and invariant curves in systems with nonmonotonic rotation number profiles.

Here, we introduce the rational standard nontwist map (RSNM), a generalization of the SNM with an additional parameter μ , which modifies the perturbation and breaks the discrete symmetry of the map.

The rational perturbing function was previously considered in the rational standard twist map (RSTM), a generalization of the STM [30]. While the perturbation in the STM and SNM is driven by a single harmonic oscillation, the perturbation in the RSTM and RSNM presented in this work is driven by a full harmonic spectrum [30]. The symmetry breaking induced by μ is of particular interest because it induces unbiased directed transport, known as the ratchet effect [31–33], where orbits exhibit a preferential direction of motion in the absence of a biasing external force. Thus, the RSNM provides a richer and more versatile framework for studying transport phenomena in nontwist systems.

In this paper, we investigate the dynamics of the RSNM, focusing on how the parameter μ affects the structure of phase space and the transport properties of the system. We begin by exploring the general behavior of the RSNM and comparing it with the SNM Sec. II, where we introduce the map, discuss the effects of the symmetry-breaking parameter and analyze the fixed points of the system. We also analyze the phase space of the RSNM for various parameter values, highlighting the changes in chaotic domains and the stability of invariant

structures. Section III delves into the role of transport barriers and examines how they evolve as the parameters are varied. We also explore how partial transport barriers influence the dynamics of chaotic orbits and analyze the conditions under which the ratchet effect occurs. The paper concludes with a discussion of our findings in Sec. IV.

II. THE RATIONAL STANDARD NONTWIST MAP: FIXED POINTS AND PHASE SPACE STRUCTURE

Many area-preserving maps can be described in the form [18]

$$y_{n+1} = y_n + \epsilon f(x_n, y_{n+1}),$$

$$x_{n+1} = x_n + \alpha(y_{n+1}) + \epsilon g(x_n, y_{n+1}),$$
 (1)

with the area preservation condition $\frac{\partial f}{\partial y_{n+1}} + \frac{\partial g}{\partial x_n} = 0$ and (y, x) a pair of canonical variables. Such maps are usually derived from a periodically kicked Hamiltonian as

$$H(x, y, t) = H_0(y) + \epsilon H_1(x, y, t),$$
 (2)

where H_0 is the unperturbed Hamiltonian, H_1 is the nonintegrable kicked perturbation with intensity controlled by ϵ . Then, the functions f and g in Eq. (1) are partial derivatives of H_1 with respect to x and y, respectively. The unperturbed frequency of the system is given by $\alpha(y) = \frac{\partial H_0(y)}{\partial y}$. The nondegeneracy condition for the frequencies of a Hamiltonian flux is $\frac{\partial^2 H_0}{\partial y^2} \neq 0$, which corresponds to the twist condition for maps: $\frac{\partial x_{m+1}}{\partial y} \neq 0$.

The standard nontwist map (SNM) can be derived from the Hamiltonian

$$H(x, y, t) = a\left(y - \frac{y^3}{3}\right) + \frac{b}{2\pi}\cos(2\pi x)\sum_{n = -\infty}^{\infty} \delta(t - n),$$

which provides $f(x, y) = -b \sin(2\pi x)$, g(x, y) = 0 and the quadratic twist function $\alpha(y) = a(1 - y^2)$. This results in the SNM as introduced in Ref. [13].

$$y_{n+1} = y_n - b \sin(2\pi x_n),$$

$$x_{n+1} = x_n + a(1 - y_{n+1}^2) \mod 1,$$
(4)

where a and b are positive real-valued parameters. The parameter a governs the nonmonotonic profile, while b determines the amplitude of the nonlinear perturbation. From Eq. (3), it is evident that the spatial dependence of the perturbation is characterized by a single harmonic. In contrast, the rational standard nontwist map (RSNM) can be obtained from the Hamiltonian

$$H(x, y, t) = a\left(y - \frac{y^3}{3}\right) - \frac{b}{2\pi\mu} \ln(1 - \mu\cos(2\pi x))$$

$$\times \sum_{n = -\infty}^{\infty} \delta(t - n), \tag{5}$$

which provides $f(x, y) = -b \frac{\sin(2\pi x)}{1 - \mu \cos(2\pi x)}$, g(x, y) = 0 and the same twist function as the SNM, $\alpha(y) = a(1 - y^2)$. The cor-

responding map is

$$y_{n+1} = y_n - b \frac{\sin(2\pi x_n)}{1 - \mu \cos(2\pi x_n)},$$

$$x_{n+1} = x_n + a(1 - y_{n+1}^2) \mod 1,$$
 (6)

where $0 \le \mu < 1$. If $\mu = 0$ in Eq. (6), the SNM (Eq. (4)) is recovered. A Fourier expansion of the nonintegrable part of the Hamiltonian given by Eq. (5) shows that it includes all harmonics in x, with the expansion coefficients decreasing geometrically. For example, see the Appendix of Ref. [30].

A map M is symmetric with respect to a transformation T if TM = MT is satisfied. The SNM obeys the following discrete symmetry transformation [25]

$$T = (x \pm \frac{1}{2}, -y).$$
 (7)

Applying the transformation (7) to the RSNM (6) to verify the condition TM = MT, we find

$$\left[x_n + a \left(1 - y_{n+1}^2 \right) \right] \pm \frac{1}{2} = \left(x_n \pm \frac{1}{2} \right) + a \left(1 - y_{n+1}^2 \right),$$

$$- \left[y_n - b \frac{\sin(2\pi x_n)}{1 - \mu \cos(2\pi x_n)} \right] = -y_n - b \frac{\sin(2\pi (x_n \pm \frac{1}{2}))}{1 - \mu \cos(2\pi (x_n \pm \frac{1}{2}))},$$
(8)

and noting that $\sin(2\pi x + \pi) = -\sin(2\pi x)$ and $\cos(2\pi x + \pi) = -\cos(2\pi x)$.

$$x_n + a(1 - y_{n+1}^2) \pm \frac{1}{2} = x_n + a(1 - y_{n+1}^2) \pm \frac{1}{2},$$

$$-y_n + b \frac{\sin(2\pi x_n)}{1 - \mu \cos(2\pi x_n)} = -y_n + b \frac{\sin(2\pi x_n)}{1 + \mu \cos(2\pi x_n)}.$$
 (9)

The second equality in Eq. (9) only holds for $\mu=0$. Choosing $\mu>0$ breaks the discrete symmetry of the map. The breaking of a spatial and/or temporal symmetry in Hamiltonian systems induces transport in a preferred direction in the phase space [31]. This phenomenon, known as the ratchet effect, has been observed in area-preserving mappings through a modified SNM that includes an additional resonant perturbation [33], as well as in drift motion $\mathbf{E} \times \mathbf{B}$ in toroidal plasma [34].

The fixed points of the RSNM are found with the conditions $y_{n+1} = y_n = y^*$ and $x_{n+1} + m = x_n = x^*$, where m is an integer number due to the periodicity of the variable x and (x^*, y^*) the coordinates of the fixed point. From Eq. (6), we see that the first condition is satisfied by $x^* = 0$ and $x^* = 1/2$, and the second condition by $y^* = \sqrt{1 + m/a}$ and $y^* = -\sqrt{1 + m/a}$. Therefore, for each integer m, sets of four fixed points are found. We compactly write the fixed points as

$$z_{nm\pm}^* = (x_{nm\pm}^*, y_{nm\pm}^*) = \left(\frac{n}{2}, \pm \sqrt{1 + \frac{m}{a}}\right),$$
 (10)

where $n \in \{0, 1\}$. These fixed points are also fixed points of the SNM, but in the RSNM their stabilities are affected by μ . The stability of a fixed point can be assessed by computing the residue [35], defined as

$$R = \frac{1}{4}(2 - \text{tr}J),$$
 (11)

TABLE I. Residues of the fixed points of the SNM and of the RSNM. Although the fixed points coordinates are the same for both maps, their residues differ.

Fixed point	SNM Residue	RSNM Residue	Stability
z_{0m+}^* z_{1m-}^*	$-\pi ab\sqrt{1+\frac{m}{a}} \\ -\pi ab\sqrt{1+\frac{m}{a}}$	$-\frac{\frac{\pi ab}{\mu - 1}\sqrt{1 + \frac{m}{a}}}{-\frac{\pi ab}{\mu + 1}\sqrt{1 + \frac{m}{a}}}$	Unstable Unstable
z_{0m-}^* z_{1m+}^*	$\frac{\pi ab\sqrt{1+\frac{m}{a}}}{\pi ab\sqrt{1+\frac{m}{a}}}$	$-\frac{\pi ab}{\mu-1}\sqrt{1+\frac{m}{a}}$ $\frac{\pi ab}{\mu+1}\sqrt{1+\frac{m}{a}}$	Parameter-dependent Parameter-dependent

where J is the Jacobian matrix of the map evaluated at the fixed point. The orbit is stable for 0 < R < 1. For the RSNM, the elements of the Jacobian matrix are

$$J_{11} = 1, (12)$$

$$J_{12} = -\frac{2\pi b \cos(2\pi x)}{1 - \mu \cos(2\pi x)} + \frac{2\pi b \mu \sin^2(2\pi x)}{(1 - \mu \cos(2\pi x))^2},$$
 (13)

$$J_{21} = -2a\left(y - \frac{b\sin(2\pi x)}{1 - \mu\cos(2\pi x)}\right),\tag{14}$$

$$J_{22} = 1 - 2a \left(y - \frac{b \sin(2\pi x)}{1 - \mu \cos(2\pi x)} \right)$$

$$\times \left(-\frac{2\pi b \cos(2\pi x)}{1 - \mu \cos(2\pi x)} + \frac{2\pi b \mu \sin^2(2\pi x)}{(1 - \mu \cos(2\pi x))^2} \right), \quad (15)$$

and $tr J = J_{11} + J_{22}$.

Analyzing the residues of the SNM's fixed points, we observe that the pair of fixed points z_{0m+}^* and z_{1m-}^* share the same residue and are unstable across all parameter configurations. In contrast, the fixed points z_{0m-}^* and z_{1m+}^* also have matching residues but can be either stable or unstable depending on the parameter values.

Turning to the RSNM, we find that the fixed points z_{0m+}^* and z_{1m-}^* remain unstable for all parameter combinations, but their residues differ. For the first, the residue is given by $R=\frac{\pi ab}{\mu-1}\sqrt{1+\frac{m}{a}}$, while for the latter, $R=-\frac{\pi ab}{\mu+1}\sqrt{1+\frac{m}{a}}$. Given that a and b are positive constants and $0<\mu<1$, we observe that both residues are negative for all parameter choices, confirming that these fixed points are unstable. For the fixed point z_{0m-}^* , we calculate the residue $R=-\frac{\pi ab}{\mu-1}\sqrt{1+\frac{m}{a}}$, which can be stable or unstable depending on the control parameters. Conversely, for the fixed point z_{1m+}^* the residue is $R=\frac{\pi ab}{\mu+1}\sqrt{1+\frac{m}{a}}$, so its stability also depends on the control parameters. A summary of the residues of fixed points for both the SNM and the RSNM is presented in Table I.

To further explore the stability of the fixed points z_{0m-}^* and z_{1m+}^* as μ increases, we analyze the behavior of these points for m=0 through 5, considering two distinct sets of parameters a and b. In Fig. 1, we plot the y-coordinates of the fixed points as a function of μ . Solid curves denote stable fixed points, while dashed curves indicate instability. The curves are color-coded according to the value of m, with blue, green, red, orange, purple, and cyan representing m=0, m=1, m=2, m=3, m=4, and m=5, respectively.

In Fig. 1(a), we set a = b = 0.2. At $\mu = 0$, all fixed points are initially stable. As μ increases, the z_{0m}^* fixed points starts

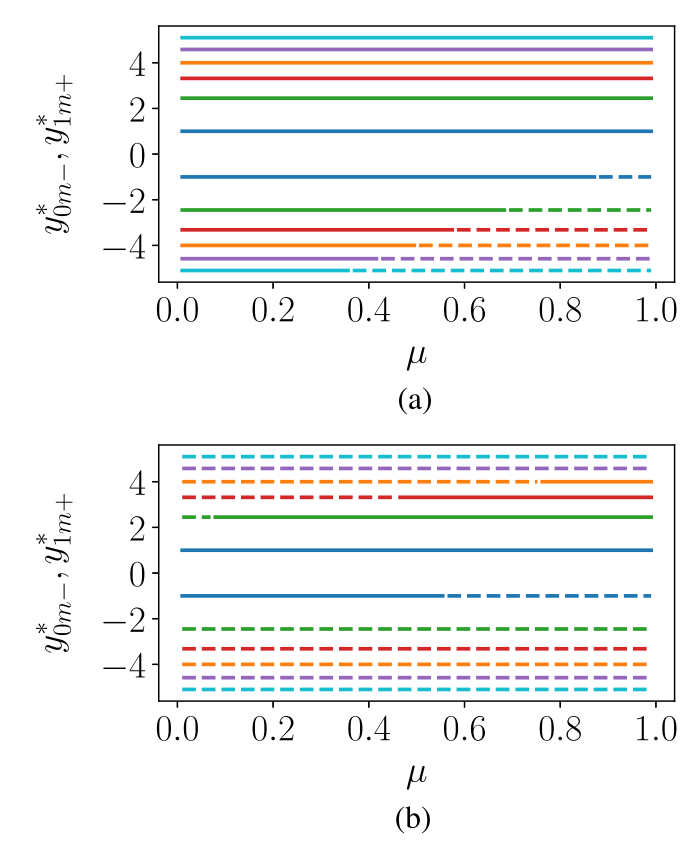


FIG. 1. Stability of the fixed points z_{0m-}^* and z_{1m+}^* , which depends on parameter values, as a function of μ for m=0 through m=5. Solid curves indicate stable fixed points, while dashed curves indicate unstable fixed points. The colors represent different values of m: blue for m=0, green for m=1, red for m=2, orange for m=3, purple for m=4, and cyan for m=5. (a) The case where a=b=0.2, starting with all fixed points stable at $\mu=0$. (b) The case where a=0.2 and b=0.7, where most fixed points are unstable at $\mu=0$.

to become unstable, with higher m values becoming unstable first. Conversely, in Fig. 1(b), where a=0.2 and b=0.7, most fixed points are unstable at $\mu=0$, except for the m=0 case. As μ increases, the z_{1m+}^* fixed points gradually become stable, starting from the lower m values. Notably, the z_{00-}^* fixed point, which is initially stable, becomes unstable as μ continues to rise.

This result regarding the stability of fixed points contrasts with the findings for the RSTM, where μ was observed to regularize the phase space structure uniformly [30]. In the RSNM, however, we find that the effect of μ is more asymmetric. Specifically, μ regularizes the upper half of the phase space by stabilizing fixed points and promoting resonance islands, while in the lower half, it leads to destabilization of fixed points, enhancing chaotic behavior.

To begin exploring the effect of the parameter μ on the phase space, we set a=b=0.2 and consider increasing values of μ . In panel (a) of Fig. 2, we start with $\mu=0$, which corresponds to the SNM. Moving to panel (b), where $\mu=0.2$, we observe that the upper region of the phase space becomes more regular, indicated by a reduction of the chaotic sea's extent. Conversely, the chaotic region in the lower part of the

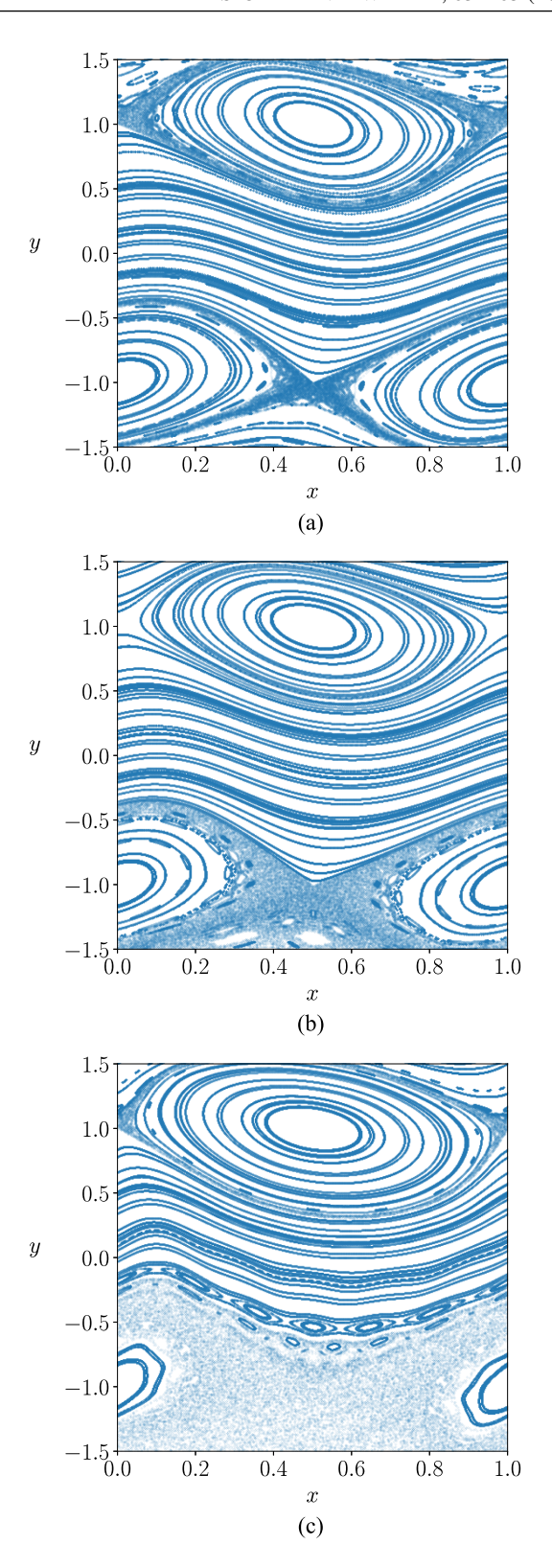


FIG. 2. Phase spaces of the RSNM for a=b=0.2 and (a) $\mu=0$, which recovers the SNM, (b) $\mu=0.2$, and (c) $\mu=0.6$. The effect of μ is to increase the chaotic domain in the lower part of the phase space and enlarge the resonance island in the upper part of the phase space.

phase space expands. In panel (c), with $\mu = 0.6$, the chaotic domain in the lower part of the phase space increases, leading to the destruction of invariant tori. A thin chaotic layer is

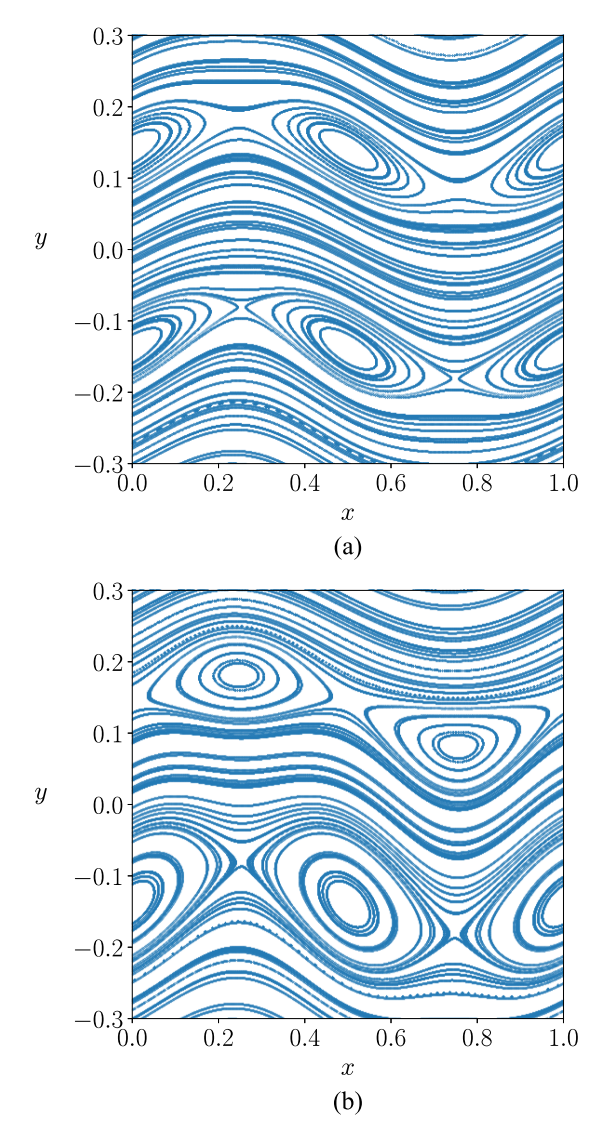


FIG. 3. Phase spaces of the RSNM for a=0.51 and b=0.1. (a) $\mu=0$, which recovers the SNM, and (b) $\mu=0.05$. The upper period-2 isochronous resonance is shifted in the RSNM.

visible in the upper phase space, though it is smaller compared to the chaotic domain observed at $\mu = 0$.

Another effect of μ is the defocusing of even-period isochronous resonances. Due to its symmetry properties, the even-period isochronous resonances in the SNM have their elliptic and hyperbolic points aligned. In the RSNM, however, we observed that as μ increases, the upper resonance chain shifts, causing the periodic orbits of same stability to become misaligned. This is illustrated in Fig. 3, where we consider a=0.51 and b=0.1. In panel (a), where $\mu=0$, we see an isochronous resonance of period two with the periodic orbits of same stability aligned. Moving to panel (b), where $\mu=0.05$, the upper chain is shifted, and the orbits become misaligned.

In the SNM, the parameter b governs the intensity of the nonlinear perturbation and the extent of chaotic domains within the phase space. In the RSNM, even low values of b can result in a highly chaotic phase space when μ is sufficiently increased. In Fig. 4, we consider a=0.45, b=0.05, and

 $\mu = 0.9$. Panel (a) displays the phase space over the range $y \in [-5, 5]$. Despite the low value of b, chaotic behavior dominates the lower half of the phase space, while large resonance island are observed in the upper half, separated by chaotic layers. The fixed points of the map with m = 0through m = 10 are shown, with their stability's assessed by the residue criterion. Stable fixed points are marked by open red circles, while unstable ones are indicated by filled red circles. In panel (b), we provide a magnified view of the region occupied by the invariant spanning curves. In both panels (a) and (b), the shearless curve is shown in red. It has been identified by the extreme in the rotation number profile, which is depicted in panel (c) and computed as $\omega = \lim_{n \to \infty} \frac{x_n - x_0}{n}$. The shearless curve divides the upper and lower regions of the phase space, with the lower region dominated by chaos and the upper region by stability islands and a wider region of spanning curves.

III. TRANSPORT DYNAMICS

As observed in the previous section, a set of invariant spanning curves acts as total transport barriers, preventing orbits in the lower chaotic sea from reaching the upper chaotic sea, and vice versa. However, increasing either b or μ leads to destruction of these curves, the shearless curve being the most resistant to perturbation and roughly the last to be destroyed.

To assess the presence of transport barriers on a wide range of parameters, the following numerical scheme was implemented. For a fixed value of μ , a grid of 500 by 500 points was constructed in the (a,b) plane. For each pair (a,b), 100 initial conditions were distributed over the line y=-5 and iterated 10^5 times. If none of these initial conditions reached the line y=5 within this time interval, a transport barrier was considered to exist and the corresponding point in the (a,b) plane was marked. This process is repeated for all points on the grid and different values of μ .

The results, depicted in Fig. 5, illustrate how varying the parameter μ influences the existence of transport barriers within the (a,b) plane. The panels show the regions where a total transport barrier is present for (a) $\mu = 0$, (b) $\mu = 0.2$, (c) $\mu = 0.4$, (d) $\mu = 0.6$, (e) $\mu = 0.8$ and (f) $\mu = 0.9$. As μ increases, the area corresponding to the presence of a transport barrier decreases. We also observed an unexpected behavior in the RSNM: the emergence of transport in previously restricted regions. This phenomenon is illustrated in panels (d), (e), and (f) of Fig. 5, where white areas appear within the blue regions. In other words, holes are created within the prohibited transport zone, leading to regions of net transport for $\mu \neq 0$.

Once the shearless curve is destroyed, transport between previously disconnected chaotic regions becomes possible. This transport can either increase or decrease with slight variations in a control parameter, suggesting the existence of a partial transport barrier. In the SNM, heteroclinic crossings between the manifolds of twin unstable orbits, along with the mechanism of turnstiles, have been shown to contribute to the observed increase in transport following the destruction of the shearless curve [23,29].

The transport across phase space regions can be quantified by the transmissivity T, which is defined as the ratio of the number of orbits that cross the barrier to the total number of

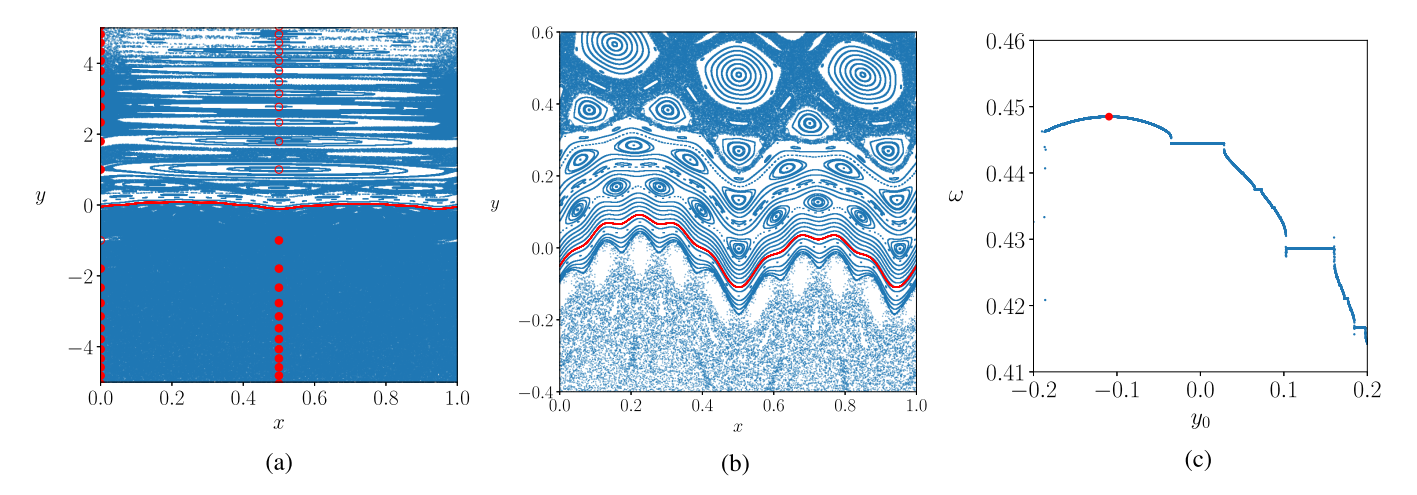


FIG. 4. (a) Phase spaces of the RSNM for a = 0.45, b = 0.05 and $\mu = 0.9$. Stable fixed points are marked by open red circles, and unstable fixed points by filled red circles. All the fixed points at either at x = 0 or x = 0.5. (b) Amplification in the vicinity of the invariant spanning curves, around y = 0. The red curve in (a) and (b) corresponds to the shearless curve, which is identified by the extreme in the rotation number profile shown in panel (c) computed for a set of y_0 with fixed $x_0 = 0.5$, where the red dot signals the maximum.

orbits within a specified time interval [23]. The direction of the motion can be determined by computing the average value of *y* over time for an ensemble of initial conditions. For the *i*-th initial condition, the time average is

$$\bar{y}_i = \frac{1}{n+1} \sum_{i=0}^{n} y_{i,j},$$
 (16)

where the j index represents the j-th iteration. Then, the average over the ensemble of M initial conditions is

$$\langle y \rangle = \frac{1}{M} \sum_{i=1}^{M} \bar{y}_i. \tag{17}$$

We calculated the transmissivity T using $M = 10^5$ initial conditions distributed along the line y = -0.9. Transport was considered to have occurred if the orbits reached the line y = 0.9. In the simulations, the parameters b = 0.1 and $\mu = 0.9$ were fixed, while the effect of the parameter a on transport was analyzed within the interval $a \in [0.73, 0.78]$. The transmissivity results are presented in Fig. 6(a), where the blue curve corresponds to n = 500 iterations, and the orange curve represents n = 1000 iterations. A transmissivity value T = 0 indicates the presence of a total transport barrier or a partial barrier that was not crossed within the given number of iterations. The observed fluctuations in transmissivity highlight the sensitivity of transport to the parameter a, pointing

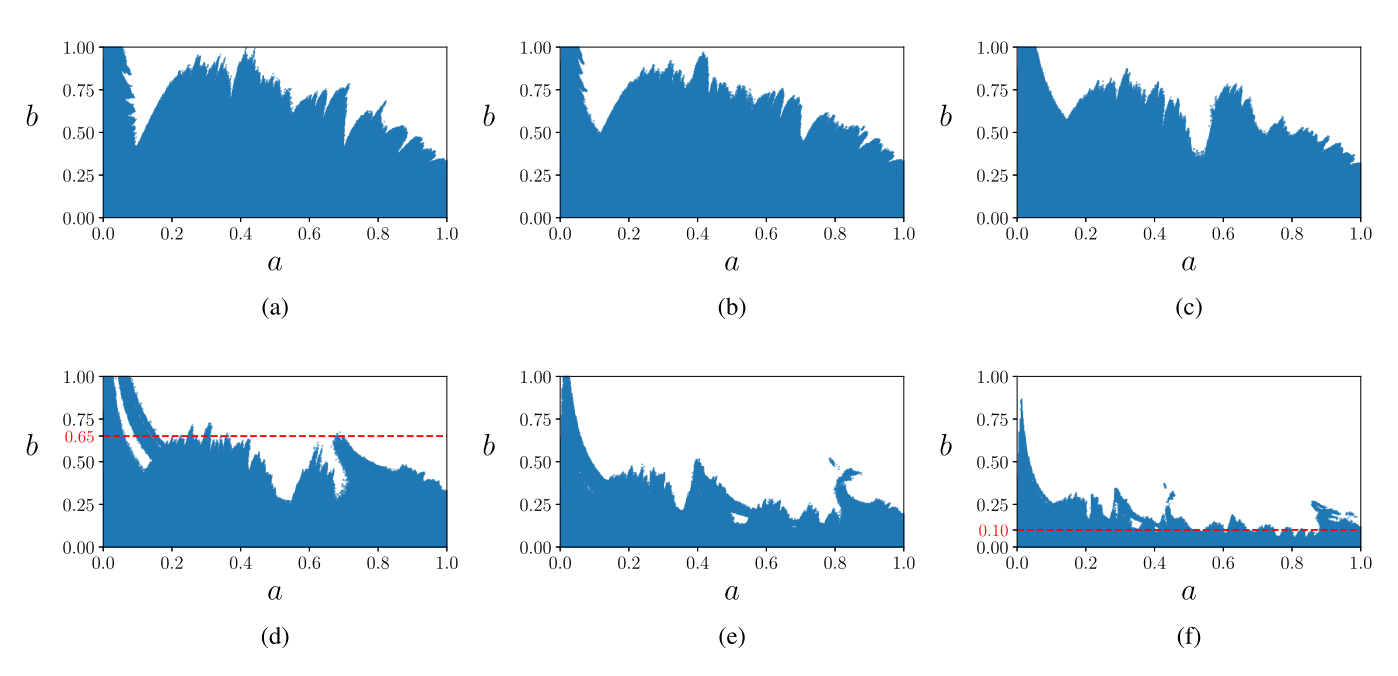


FIG. 5. Diagrams for the existence of a transport barrier (represented in blue points) in the phase space for different values of μ : (a) $\mu = 0$, (b) $\mu = 0.2$, (c) $\mu = 0.4$, (d) $\mu = 0.6$, (e) $\mu = 0.8$, and (f) $\mu = 0.9$. The horizontal red lines in panels (d) and (f) indicate the value of b considered in Fig. 9 and Fig. 6, respectively.

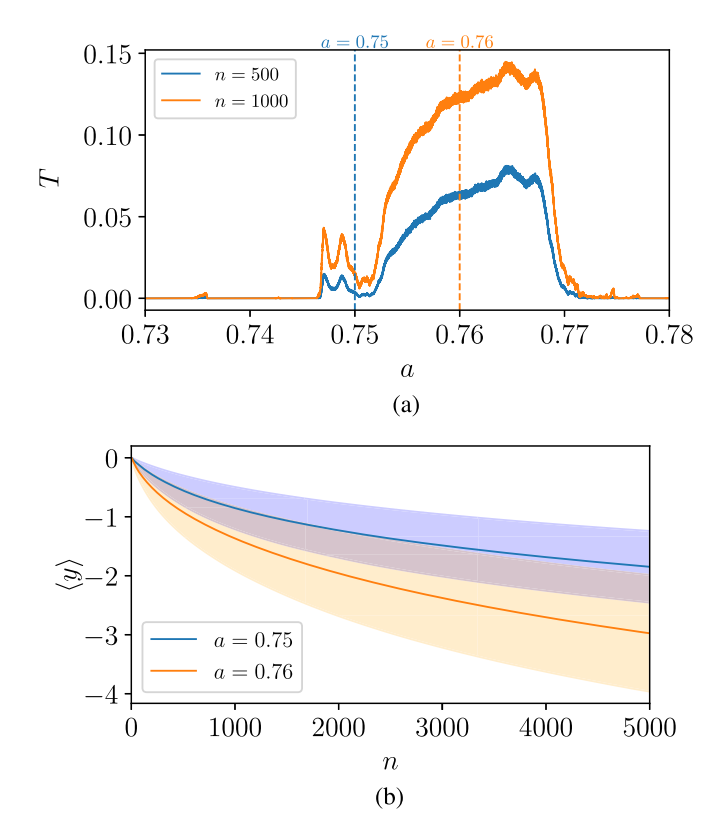


FIG. 6. (a) Transmissivity of the RSNM for b=0.1 and $\mu=0.9$, for times n=500 (blue) and n=1000 (orange). (b) Average value of y as a function of iteration number and 10^5 initial conditions for the RSNM with b=0.1, $\mu=0.9$. The blue curve corresponds to a=0.75, where a partial transport barrier is observed, while the orange curve corresponds to a=0.76, where no transport barrier exists. The shaded regions correspond to the standard deviation. Note that the overlap of the shaded regions between the curves may give the impression of a third color, but this is simply a visual result of the intersection and not a separate data set. On average, the orbits tend to move downward in the phase space.

to the existence of a partial transport barrier. To investigate whether transport exhibits a preferred direction under conditions of low and high transmissivity, we selected a = 0.75for low transmissivity and a = 0.76 for high transmissivity. We emphasize that these two cases were arbitrarily chosen to illustrate the differences in transmissivity. However, many other peaks in transmissivity, including those before a = 0.75, arise due to a non-smooth dependence on the parameter [23]. Nonetheless, the scenarios remain essentially the same for the two cases that we present. For each case, $M = 10^5$ initial conditions were uniformly distributed along the line y = 0and evolved over n = 5000 iterations. The average value $\langle y \rangle$ was calculated after each iteration using Eq. (17). The results, shown in Fig. 6(b), reveal a consistent downward drift in phase space for both cases, with lower values of $\langle y \rangle$ observed in the absence of a partial barrier.

To further investigate the phase space structure associated with the previously selected cases of low and high transmissivity (a = 0.75) and (a = 0.76), respectively, the corresponding phase spaces are shown in Fig. 7. Panel (a) illustrates the low transmissivity scenario, while panel (b)

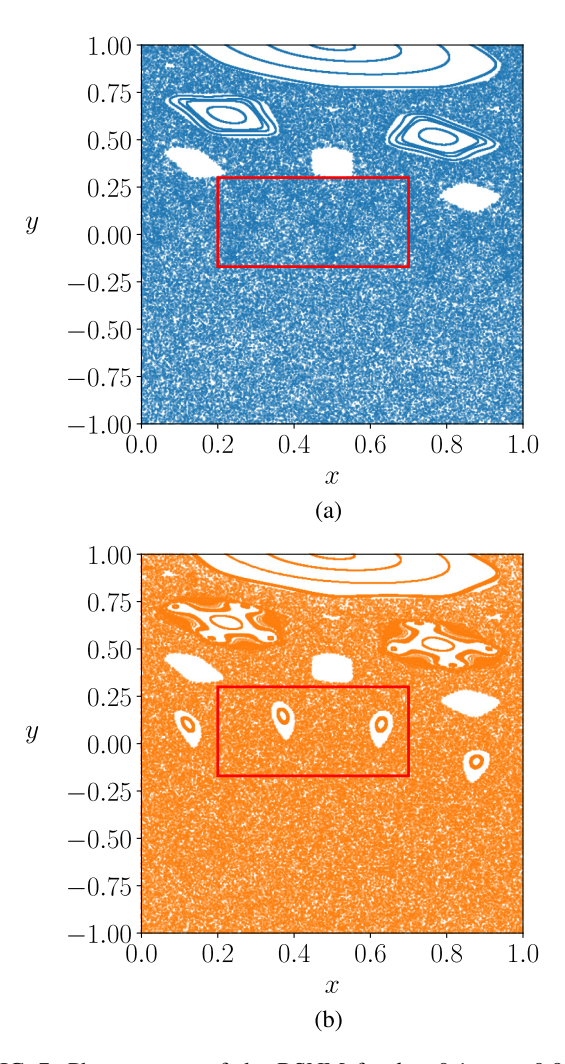


FIG. 7. Phase spaces of the RSNM for b=0.1, $\mu=0.9$ and (a) a=0.75 (low transmissivity) and (b) a=0.76 (high transmissivity). The red-boxed region are analyzed in Fig. 8 with the Lagrangian descriptor.

represents the high transmissivity scenario. The primary difference between these configurations is the appearance of a period-4 resonance island in the high transmissivity case.

Building on the analysis of the phase space structures, we focus on the red-boxed regions highlighted in Fig. 7 to investigate the mechanism behind the increased transmissivity. In these regions, the Lagrangian descriptor (LD) is computed to visualize the geometry of the invariant manifolds. The LD is a scalar quantity that reveals phase space structures such as stable and unstable manifolds and the separatrices of hyperbolic equilibria. It is determined by calculating the arc length of trajectories over a finite size time window [36–40]. For maps, the LD of an initial condition (x_0, y_0) over a time interval -n to n is defined as [41–43]

$$LD(x_0, y_0; n) = \sum_{i=-n}^{n} \sqrt{|x_{i+1} - x_i|^2 + |y_{i+1} - y_i|^2}.$$
 (18)

The LD is effective in reconstructing finite segments of the invariant manifolds associated with hyperbolic equilibria, with the manifolds' locations identified by abrupt changes in

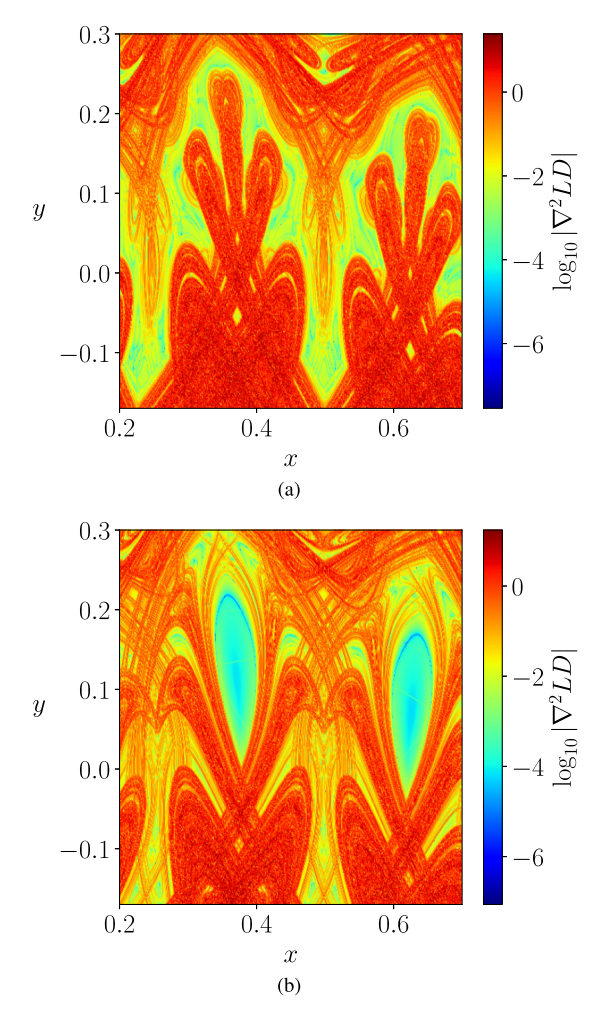
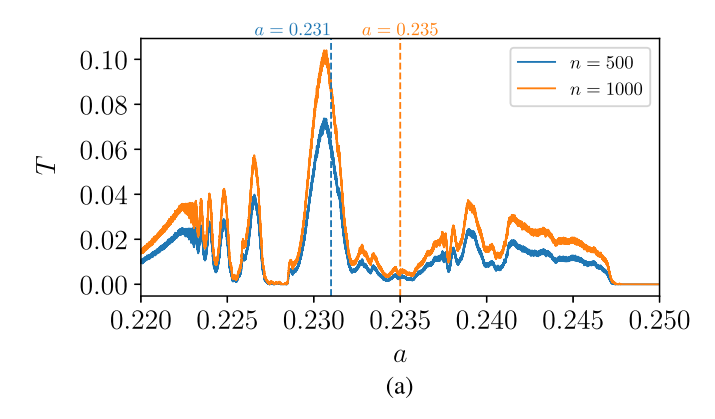


FIG. 8. Laplacian of the LD computed over phase space regions of the RSNM for b=0.1, $\mu=0.9$ and (a) n=25 and a=0.75, showing low transport and no crossings between the manifolds in the upper and lower phase space regions, and (b) n=20 and a=0.76, showing high transport with crossings between the manifolds in the upper and lower phase space regions.

the LD value [44]. As LD is nondifferentiable when crossing transversely hyperbolic domains [3,42], quantifying its regularity enhances the visualization of the hyperbolic structures. This is achieved by computing the Laplacian of the LD [3,42,43]. This is illustrated in Fig. 8, where $|\nabla^2 LD|$ was calculated for the red-boxed regions of the phase spaces shown in Fig. 7 and plotted in log scale. In the low transmissivity case (panel (a), with a = 0.75) the invariant manifolds in the upper phase space region do not cross those in the lower phase space region. Conversely, in the high transmissivity case (panel (b), with a = 0.76) the manifolds in the upper phase space region do cross those in the lower region, indicating that the increase in transmissivity is due to the turnstile mechanism and intercrossing between the islands [29]. We also included a Supplemental Material animation [45], where the top panel shows the $|\nabla^2 LD|$ plot and the bottom panel displays the transmissivity as a function of the parameter a. It is clear that the higher values of $|\nabla^2 LD|$ reveals the geometry of the invariant manifolds, which connect and disconnect the upper



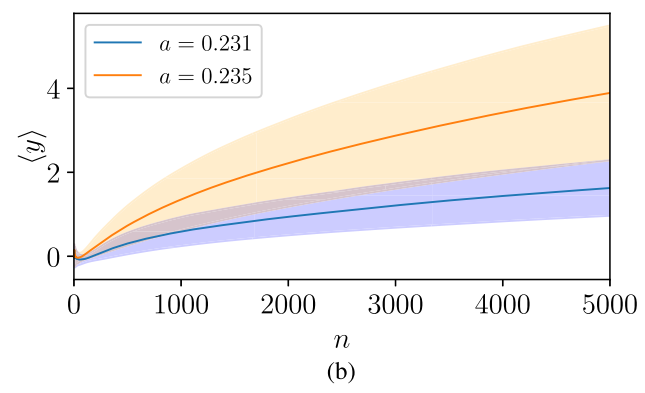


FIG. 9. (a) Transmissivity of the RSNM for b = 0.65 and $\mu = 0.6$, for times n = 500 (blue) and n = 1000 (orange). (b) Average value of y for a = 0.231 (blue) and a = 0.235 (orange).

and lower section of the phase space, playing a crucial role in transport.

Although the result of Fig. 6 suggests that the ratchet effect is improved by the absence of a partial transport barrier, this is not the case. For a counter-example we consider b=0.65, $\mu=0.6$ and vary a within the interval $a\in[0.73,0.78]$ to compute the transmissivity as described previously. This is shown in Fig. 9(a), and again we choose a configuration of high transmissivity, a=0.231, and a configuration with low transmissivity, a=0.235. In Fig. 9(b) we show the average $\langle y \rangle$ for those two configurations, and observe that the net transport is higher in the case of low transmissivity and that there is an upward drift in phase space for both cases.

To explore the influence of μ in the transport direction on a wide range of parameters, we constructed grids of 500 by 500 points in the (a, b) plane for fixed values of μ . For each grid points, we compute the average $\langle y \rangle$ after $n = 10^4$ iterations, using M = 100 initial conditions. This analysis was restricted to parameter combinations where no transport barrier was detected, based on the scheme implemented in Fig. 5. The results are presented in Fig. 10, with panels (a), (b), (c), and (d) corresponding to $\mu = 0.4$, $\mu = 0.6$, $\mu = 0.8$, and $\mu = 0.9$, respectively. In these plots, the black region indicates points where a total transport barrier was identified. Green dots correspond to parameters for which $|\langle y \rangle| < 0.01$, suggesting minimal net transport. This can be caused by a partial transport barrier or strong stickiness. The color scale from red to blue corresponds to positive and negative $\langle y \rangle$, respectively. Blue regions, indicating negative net transport

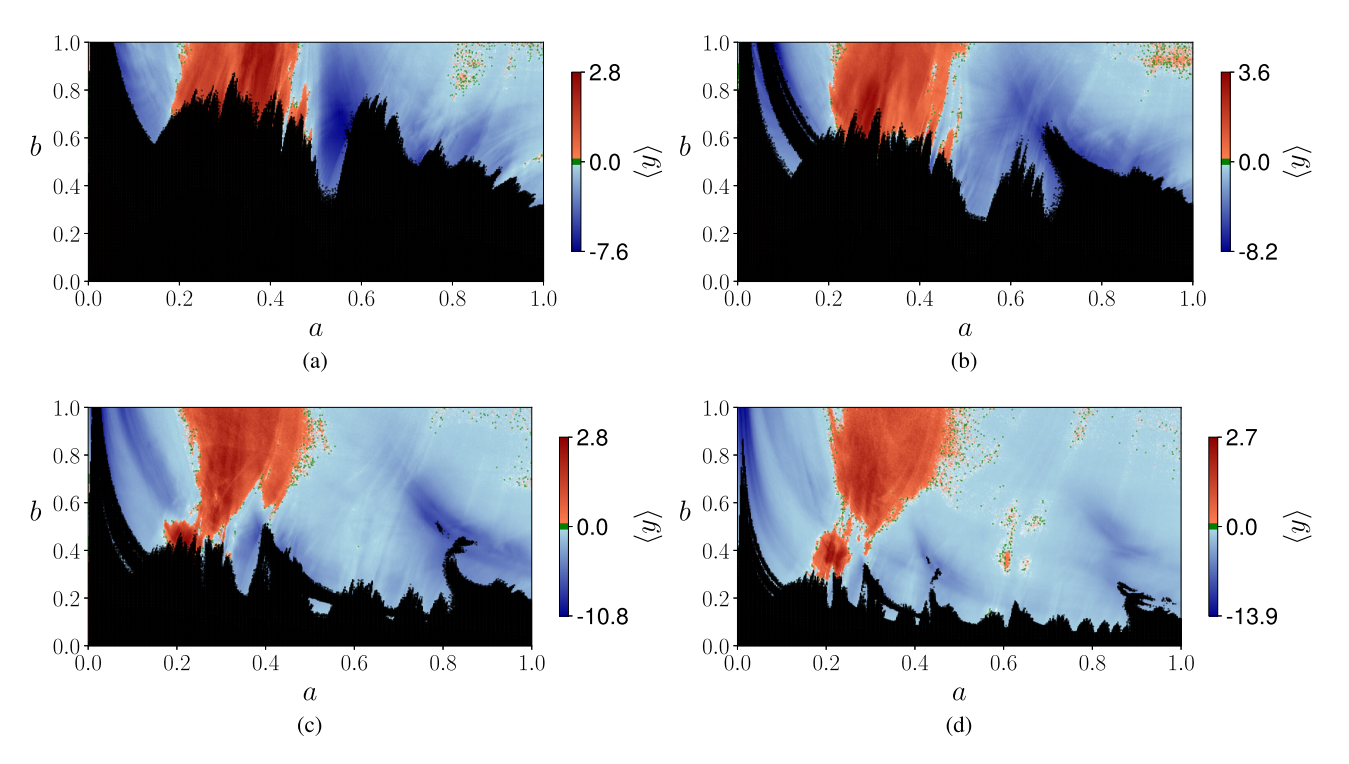


FIG. 10. Projection of $\langle y \rangle$ in the parameter space (a, b), exhibiting positive or negative net transport, in red and blue colors, respectively, for different values of μ . Black region corresponds to a total transport barrier, and green points to $|\langle y \rangle| < 0.01$, indicating low net transport. (a) $\mu = 0.4$, (b) $\mu = 0.6$, (c) $\mu = 0.8$, and (d) $\mu = 0.9$.

in the y variable, are prominent across the parameter space. In contrast, the red region, which corresponds to positive net transport, is comparatively small. We also observe that the ratchet leading to negative net transport reaches higher y absolute values than the one leading to positive net transport. This is due to the stickiness effect that occurs in the upper half of the phase space, as the parameter μ tends to stabilize the fixed points in that region and creates resonance islands.

IV. CONCLUSIONS

In this study, we have explored the dynamics and transport properties of the rational standard nontwist map (RSNM), a generalization of the standard nontwist map (SNM), by introducing a perturbation parameter μ that breaks the symmetry of the map. This symmetry breaking leads to significant modifications in the phase space structure and introduces the phenomenon of unbiased directed transport, commonly known as the ratchet effect.

Our analysis began by examining the effects of the parameter μ on the fixed points of the map. Additionally, we demonstrated that the stability of fixed points in the RSNM is affected by μ , which alters the phase space significantly compared to the SNM.

We observed that as μ increases, the upper region of the phase space becomes more regular while the chaotic domain in the lower region expands, leading to the destruction of invariant spanning curves. We also observed that μ leads to the defocusing of even-period isochronous resonances, which are always aligned in the SNM and becomes misaligned even for relatively small values of μ in the RSNM. Furthermore, the

introduction of μ allows the creation of holes in the parameter space within the prohibited transport zone. This, in turn, enables the discovery of new regions of net transport that were previously unanticipated in the SNM.

We then focused on the role of invariant spanning curves as transport barriers, showing that their destruction, particularly the shearless curve, is a critical factor in enabling transport between different regions of the phase space. In addition to the complete destruction of transport barriers, we also identified the presence of partial transport barriers in the RSNM. These partial barriers still limit transport across the phase space but allow for some degree of interaction between the chaotic regions above and below them. The transmissivity analysis provided insight into how transport varies with the control parameters, revealing that even small changes in these parameters can lead to significant differences in transport behavior. The increase in transport observed with small variations in the parameter a is related to the mechanism of turnstiles, which are formed by the crossing of stable and unstable manifolds from different regions of the phase space. These turnstiles facilitate the exchange of orbits between the upper and lower regions, effectively acting as gateways that enhance transport. As a result, even slight adjustments to the system's parameters can lead to significant changes in the overall transport dynamics.

Finally, we investigated the directed transport in the RSNM by calculating the average displacement $\langle y \rangle$ of chaotic orbits over time. Our results indicate that the symmetry breaking induced by μ leads to a preferential direction of transport, with negative net transport being predominant in the parameter space.

In conclusion, the RSNM presents a rich structure for studying transport phenomena in nontwist Hamiltonian systems. The introduction of the perturbation μ generalizes the SNM and opens up new possibilities for understanding directed transport mechanisms.

ACKNOWLEDGMENTS

This study was supported by the the Araucária Foundation, Brazil, the Coordination for the Improvement of Higher Education Personnel (CAPES), Brazil–Finance Code 001, the

- National Council for Scientific and Technological Development (CNPq), Brazil, under Grants No. 309670/2023-3 and No. 304616/2021-4, and the São Paulo Research Foundation (FAPESP), Brazil, under Grants No. 2018/03211-6, No. 2019/07329-4, No. 2024/04557-4, and No. 2024/14825-6.
 - The authors have no conflicts to disclose.

DATA AVAILABILITY

The data that support the findings of this article are openly available [46].

- V. M. de Oliveira, P. A. Sousa-Silva, and I. L. Caldas, Celest. Mech. Dyn. Astron. 132, 51 (2020).
- [2] A. Celletti, J. Gimeno, and M. Misquero, J. Nonlinear Sci. 32, 88 (2022).
- [3] J. Daquin and C. Charalambous, Celest. Mech. Dyn. Astron. 135, 31 (2023).
- [4] N. Callegari, Commun. Nonlinear Sci. Numer. Simul. 138, 108224 (2024).
- [5] P. J. Morrison, Rev. Mod. Phys. 70, 467 (1998).
- [6] P. J. Morrison, Phys. Plasmas 7, 2279 (2000).
- [7] J. D. da Fonseca, D. Del-Castillo-Negrete, and I. L. Caldas, Phys. Plasmas 21, 092310 (2014).
- [8] R. L. Viana, M. Mugnaine, and I. L. Caldas, Phys. Plasmas 30, 090901 (2023).
- [9] J. D. Meiss, Rev. Mod. Phys. 64, 795 (1992).
- [10] B. V. Chirikov, Phys. Rep. 52, 263 (1979).
- [11] J. B. Weiss, Phys. Fluids **3**, 1379 (1991).
- [12] J. E. Howard and S. M. Hohs, Phys. Rev. A 29, 418(R) (1984).
- [13] D. del-Castillo-Negrete and P. J. Morrison, Phys. Fluids A 5,
- [14] D. del-Castillo-Negrete, Phys. Plasmas 7, 1702 (2000).
- [15] J. S. Portela, I. L. Caldas, R. L. Viana, and P. J. Morrison, Int. J. Bifurc. Chaos 17, 1589 (2007).
- [16] I. L. Caldas, R. L. Viana, J. D. Szezech, Jr., J. S. E. Portela, J. Fonseca, M. Roberto, C. G. L. Martins, and E. J. da Silva, Commun. Nonlinear Sci. Numer. Simul. 17, 2021 (2012).
- [17] M. Roberto, E. C. D. Silva, I. L. Caldas, and R. L. Viana, Braz. J. Phys. 34, 1759 (2004).
- [18] A. J. Lichtenberg and M. A. Lieberman, *Regular and Chaotic Dynamics* (Springer-Verlag, New York, 1992), Vol. 2.
- [19] J. N. Mather, Topology 21, 457 (1982).
- [20] S. Aubry and P. L. Daeron, Physica D 8, 381 (1983).
- [21] R. S. MacKay, Nonlinearity 5, 161 (1992).
- [22] A. Delshams and R. de la Llave, SIAM J. Math. Anal. 31, 1235 (2000).
- [23] J. D. Szezech, I. L. Caldas, S. R. Lopes, R. L. Viana, and P. J. Morrison, Chaos 19, 043108 (2009).
- [24] R. Egydio de Carvalho and A. M. Ozorio de Almeida, Phys. Lett. A 162, 457 (1992).
- [25] D. Del-Castillo-Negrete, J. M. Greene, and P. J. Morrison, Physica D 91, 1 (1996).
- [26] R. S. MacKay, J. D. Meiss, and I. C. Percival, Phys. Rev. Lett. 52, 697 (1984).

- [27] J. D. Meiss, Chaos: An Interdiscip. J. Nonlinear Sci. 25, 097602 (2015).
- [28] M. Mugnaine, I. L. Caldas, J. D. Szezech, R. L. Viana, and P. J. Morrison, Phys. Rev. E 110, 044201 (2024).
- [29] M. Mugnaine, A. C. Mathias, M. S. Santos, A. M. Batista, J. D. Szezech, Jr., and R. L. Viana, Phys. Rev. E 97, 012214 (2018).
- [30] P. M. Cincotta and C. Simó, Physica D 413, 132661 (2020).
- [31] J. Gong and P. Brumer, Phys. Rev. E 70, 016202 (2004).
- [32] M. F. Carusela, A. J. Fendrik, and L. Romanelli, Physica A 388, 4017 (2009).
- [33] M. Mugnaine, A. M. Batista, I. L. Caldas, J. D. Szezech, Jr., and R. L. Viana, Chaos **30**, 093141 (2020).
- [34] M. Rolim Sales, D. Borin, L. C. de Souza, J. D. Szezech, Jr., R. L. Viana, I. L. Caldas, and E. D. Leonel, Chaos Solitons Fractals 189, 115614 (2024).
- [35] J. M. Greene, J. Math. Phys. 20, 1183 (1979).
- [36] J. A. J. Madrid and A. M. Mancho, Chaos: An Interdiscip. J. Nonlinear Sci. 19, 013111 (2009).
- [37] C. Mendoza and A. M. Mancho, Phys. Rev. Lett. 105, 038501 (2010).
- [38] F. Revuelta, R. M. Benito, and F. Borondo, Phys. Rev. E 99, 032221 (2019).
- [39] F. Revuelta, F. J. Arranz, R. M. Benito, and F. Borondo, Commun. Nonlinear Sci. Numer. Simul. 123, 107265 (2023).
- [40] M. D. Forlevesi, R. Egydio de Carvalho, and E. F. de Lima, Phys. Rev. E 107, 024209 (2023).
- [41] C. Lopesino, F. Balibrea, S. Wiggins, and A. M. Mancho, Commun. Nonlinear Sci. Numer. Simul. **27**, 40 (2015).
- [42] J. Daquin, R. Pédenon-Orlanducci, M. Agaoglou, G. García-Sánchez, and A. M. Mancho, Physica D 442, 133520 (2022).
- [43] R. Simile Baroni and R. Egydio de Carvalho, Phys. Rev. E **109**, 024202 (2024).
- [44] A. M. Mancho, S. Wiggins, J. Curbelo, and C. Mendoza, Commun. Nonlinear Sci. Numer. Simul. 18, 3530 (2013).
- [45] See Supplemental Material at http://link.aps.org/supplemental/ 10.1103/PhysRevE.111.034203 for the animation showing the evolution of $|\nabla^2 LD|$ and the transmissivity as the parameter a increases.
- [46] Oscillations Control Group (2025). Index of /OscilControl-Data/RationalSNM, Oscillations Control Group Data Repository, http://henon.if.usp.br/OscilControlData/RationalSNM/